A General Fruit Acid Chelation Route for Eco-friendly and Ambient 3D Printing of Metals

Soo Young Cho
Yonsei University
Dong Hae Ho
Yonsei University
Yoon Young Choi
Yonsei University
Soomook Lim
Sungkyunkwan University
Sungjoo Lee
Sungkyunkwan University https://orcid.org/0000-0003-1284-3593
Ji Won Suk
Sungkyunkwan University
Jeong Ho Cho (jhcho94@yonsei.ac.kr)
Yonsei University

Article

Keywords: additive manufacturing, metal 3D printing, binder jetting 3D printing, eco-friendly, metal-chelate bridge

Posted Date: March 17th, 2021

DOI: https://doi.org/10.21203/rs.3.rs-310961/v1

Version of Record: A version of this preprint was published at Nature Communications on March 7th, 2022. See the published version at https://doi.org/10.1038/s41467-021-27730-6.

Abstract

Recent advances in metal additive manufacturing (AM) have provided new opportunities for the design of prototypes of metal-based products and personalization of products for the fourth industrial revolution. Although metal AM, which enables fabrication of varied and sophisticated objects, is in the spotlight as a next-generation printing method, environmental issues arising during the printing process need to be addressed before it can be commercialized. Here, we demonstrate a novel mechanism for binder jetting three-dimensional (3D) printing of metals that is based on chelation triggered by an eco-friendly binding agent. Sodium salts of fruit acid chelators are used to form stable metal-chelate bridges between metal particles, which enable elaborate metal 3D printing. The strength of the 3D-printed object is improved by post-treatment, through a reduction in the porosity between the metal particles. Finally, the compatibility of the novel printing mechanism with a variety of metals is demonstrated via successful 3D printing of objects of various shapes using various metal powders. The proposed mechanism for metal 3D printing is expected to open up new avenues for the development of domestic-scale desktop 3D printing of metals.

Introduction

Additive manufacturing (AM), also known as 3D printing, is one of the most important technologies in the fourth industrial revolution because it can enable personalization of products and rapid prototyping. In an attempt to expand the boundaries of AM, numerous researchers have focused on developing printable materials[1-3] and corresponding techniques for three-dimensional (3D) printing[4-7]. Consequently developed advanced and sophisticated printable materials and 3D printing techniques have accelerated the utilization of AM in various industries, such as aerospace[8,9], biomedicine[10-12], and the food industry[13,14]. Research on metal AM that can facilitate its application to various industrial fields has also been actively conducted[15-18]. However, unlike polymer AM, metal AM still has applicability only at the industrial and academic scales because of the demanding conditions of the printing environment, which hinder realization of domestic-scale desktop applications. Selective laser melting and electron beam melting have been proposed as breakthrough technologies[19-21], but printing processes requiring high-power energy sources, inert gas atmospheres, and high-temperature preheating have limited their application range[22].

Binder jetting 3D printing (BJM3DP) is a promising AM technique that selectively jets a liquid binding agent onto metal powder, which results in bond formation between particles[23-25]. The printing process in this technique does not include a thermal sintering process[26,27], which would require a highly specialized environment and equipment. The ambient conditions of this printing process provide accessibility even to nonprofessionals[28,29]. Additionally, BJM3DP has the highest ability to enable personalization as it can be downsized using customized kits and commercially available ink cartridges. Despite such benefits of BJM3DP, it has not yet been commercialized, because of concerns about environmental and safety issues resulting from the use of binding agents. Two commonly used hazardous binding agents, 2-

butoxyethanol-based solution and 2-pyrrolidone-based solution, have been specifically considered to be responsible for such issues[30,31]. Additionally, the recently developed metal-organic dispersion ink composed of cupric formate and octylamine has also been found to have an adverse environmental impact[32,33]. Therefore, to enable domestic-scale desktop application of BJM3DP, it is essential to develop a binding agent that is eco-friendly as well as nonhazardous[24, 34-36].

Here, we introduce a novel binding mechanism for BJ3MDP that is based on the use of a chelator composed of salts of naturally available fruit acids as an eco-friendly binding agent. Metal-chelate bridges between metal particles are successfully formed *via* ink-jetting of water onto a powder composed of a uniform mixture of the metal particles and chelator. This metal-organic complexing mechanism is thoroughly analyzed by Fourier transform infrared (FT-IR) spectroscopy, X-ray photoelectron spectroscopy (XPS), and scanning electron microscopy (SEM). Then, compression tests are performed on the metal 3D-printed object to confirm the dependence of its mechanical strength on the type of chelator. Subsequently, the mechanical strength is further improved by post-treatment. Finally, objects of various shapes are printed using various metals, which demonstrates that the proposed chelator-assisted BJM3DP technique is not only useful for the realization of complex and sophisticated architectures but also applicable to a wide range of metal powders. The environmentally friendly chelator presented herein is expected to promote the desktop use of metal 3D printers (*i.e.*, on the domestic scale) by creating an environment in which even nonprofessionals can easily and safely perform 3D printing.

Results

Eco-friendly BJM3DP

Figure 1a shows the 3D scheme of the BJM3DP system, which has four main components: an inkjet cartridge, powder gantry boxes, a roller, and x- and y-axes stages. Prior to the 3D printing process, the powder and inkjet cartridge were prepared as follows (see **Supplementary Fig. 1** for photographic images of each component). First, the metal powder was mixed with the chelator. Here, the nozzle clogging issue was prevented by avoiding use of a generally preferred method of jetting a binding agent solution, which precipitates inside the inkjet cartridge and clogs the printing nozzle. Next, two gantry boxes were filled with the mixture of the metal powder and chelator. Each of these gantry boxes has a different purpose. One is the builder gantry box in which objects are 3D-printed, and the other is the feeder gantry box that stores and supplies the powder to the builder gantry box. Then, the inkjet cartridge was filled with deionized (DI) water, which activated the chelation reaction. After the preparation process, the printing cycle was initiated through deposition of a powder layer on top of the builder gantry box. During the printing process, the builder platform moved one step downward to provide space for one powder layer and the feeder platform simultaneously moved one step upward to push up the powder. Then, the roller module positioned at the feeder gantry box moved toward the builder gantry box to supply powder and flatten powder protruding on top of the latter box, as shown in **Figure 1b**. Once a powder layer was deposited, the module returned to its original position. Subsequently, DI water was jetted from the inkjet cartridge onto the powder layer deposited on top of the builder gantry box at programmed positions

(**Figure 1c**). This cyclic process was repeated until the uppermost layer of the designed 3D object was deposited. Upon completion of the printing cycle, the 3D-printed object was removed from the pile of metal powder and the unchelated powder was subsequently removed through air blowing. Photographic images of the overall metal 3D printing process are shown in **Supplementary Fig. 2.**

As binding agents, nature-based chelators, which are crucial to ensure eco-friendliness of metal 3D printing, were used. Unlike polymer binding agents, which are hazardous, the chelators utilized here are food-grade organic materials because they are salts of nature-based fruit acids (e.g., of fruits such as lemons, cherries, and grapes)[37]. For example, citric acid derived from citrus fruits has three carboxyl groups, and it transforms into sodium citrate upon replacement of the hydrogens in these groups with sodium ions through a salt-formation reaction (**Figure 1d**)[38]. Here, the carboxyl group of sodium citrate plays an important role in the metal chelation reaction. Upon wetting of the uniform mixture of the metal powder and chelator (**Figure 1e**), metal chelation occurs on the surface of the metal particles, which induces the formation of metal-chelate bridges between the particles. **Figure 1f** and **Supplementary Fig. 3** show the chemical structure of metal-chelate bridges formed on metal particle surface and the change in the microstructure of Al powder. Successful chelation imparts structural integrity to the 3D-printed object and its architecture is consequently maintained, as a result of which the object has a precise and sophisticated shape, as shown in **Figure 1g**.

Formation of metal-chelate bridges between metal particles.

Figure 2a shows the mechanism of chelate complex formation between Al particles and the underlying chemical reaction. When water droplets are jetted onto Al powder, water permeates between the particles and gradually dissolves the chelator. Then, the ionized chelator solution preferentially attacks intrinsic defects in the Al particles, consequently producing Al-chelate compounds, which results in bridging of the Al particles. **Figure 2b** shows FT-IR spectra of Al objects printed using the following proposed chelators: sodium salts of citrate (NaCit), tartrate (NaTar), succinate (NaSuc), and ascorbate (NaAsc). These four chelators have three, two, two, and one coordinate donor sites, respectively, and the difference in the number of coordination sites affects the formation of metal-chelate bridges. In the spectra of the carboxyl-based chelators (NaCit, NaTar, and NaSuc), two major bands, which originate from the asymmetric stretching vibration ($\nu_{as}(COO^-)$) and symmetric stretching vibration ($\nu_s(COO^-)$) of the carboxylate group (COO^-), are present in the frequency ranges of 1540–1720 cm^{-1} and 1320–1470 cm^{-1}, respectively[39]. In the spectra of NaCit, $\nu_{as}(COO^-)$ at 1592 cm^{-1} and $\nu_s(COO^-)$ at 1393 cm^{-1} are blue-shifted by 4 cm^{-1} and red-shifted by 11 cm^{-1}, respectively, after chelation. The increase in the molecular mass due to the chelation of the carboxylate group and Al causes a change in the vibration frequency, which results in a band shift[40]. The peak shifts of $\nu_{as}(COO^-)$ and $\nu_s(COO^-)$ thereby indicate the formation of the chelate complex on the Al particle surface (the FT-IR spectrum of pristine Al powder in the same frequency range is shown in **Supplementary Fig. 4**). The separation of peaks ($\Delta\nu = \nu_{as} - \nu_s$) was further analyzed to

identify the difference in the types of coordination between Al and the carboxyl-based chelators[41]. Because NaCit, NaTar, and NaSuc chelated with Al have a lower value of $\Delta\nu(COO^-)$ than do the chelators themselves (**Supplementary Table 1**), these chelators coordinate with Al in the bidentate chelating form, which enables a single metal atom to have two bonds with a carboxylate group, as illustrated in the left panel of **Figure 2b**. Unlike with these carboxylate-based chelators, NaAsc forms only a single bond with the Al atom, as indicated by the non-split $\nu_{C=O}$, the band broadening of ν_{C-O}, and the decreased intensity of the hydroxyl group after chelation[42].

The XPS spectra of chelated Al provide information about the extents of chelate complex formation when the different chelators are used. The left panel of **Figure 2c** and **Supplementary Fig. 5** show the Al 2p and O 1s spectra of the chelated and pristine Al powders, respectively. The deconvoluted Al 2p spectra have three distinct components: Al $2p_{3/2}$ (71.6 eV), Al $2p_{1/2}$ (72.0 eV), and Al–O (74.2 eV). The Al–O peak originates from the oxides and hydroxides formed on the Al surface[43]. As depicted in **Figure 2d**, the four types of chelated Al show a larger Al–O/Al–Al atomic ratio than the pristine Al particles. Furthermore, the atomic ratio increases as the number of coordination bonds increases. These results indicate that the chelators play a pivotal role in Al–O formation, and greater the number of coordination bonds, higher is the thickness of the Al–O layers formed on the Al particle surface, as observed in the SEM images (right panel of **Figure 2c**). This tendency of formation of a thicker Al–O layer is also confirmed from the O 1s spectra. The O 1s peak has three components, which correspond to O–Al, HO–Al, and the chemisorbed water and are positioned at 530.7, 531.8, and 532.4 eV, respectively[44]. As can be seen from the plot in **Figure 2d**, the relative amount of O–Al increases as the number of coordination bonds increases; this trend reveals that a chelator with more coordination sites is favorable for the formation of the Al-chelate complex. The promoted chelation results in stronger bonding between the metal particles, and therefore, increases the mechanical strength of the 3D-printed objects (**Figure 2e**). The object printed using NaCit has the highest compressive strength (0.88 MPa) and compressive modulus (40.66 MPa). The outstanding mechanical properties of this 3D-printed object can be explained by the fact that coordinate donor sites contribute to the strength of the 3D-printed object. Changes in the atomic ratio and mechanical properties with the type of chelator because of the difference in the number of coordination groups are depicted in **Supplementary Fig. 6**. NaCl was subsequently added to release more metal ions from the intrinsic defects in the Al particles and increase the binding strength of the printed object. Upon the addition of NaCl, the chloride ions attacked the Al defects to form Al ions, which, in turn, promoted chelation on the surface of the metal particles in an aqueous environment (**Supplementary Fig. 7**)[45]. The enhancement of chelation through NaCl addition was also confirmed by SEM, FT-IR spectroscopy, and XPS (**Supplementary Fig. 8** and **Supplementary Fig. 9**), all of which revealed numerous metal-chelate bridges. The increase in the density of metal-chelate bridges, in turn, led to an increase in the compressive modulus to 68.36 MPa; this is a 1.7-fold increase compared to that of the 3D-printed object not treated with the NaCl additive, as shown in **Supplementary Fig. 10**.

Various objects 3D-printed using NaCit chelator.

To demonstrate the elaborateness of our developed BJM3DP system, we designed and 3D-printed various 3D structures, as shown in **Figure 3a** and **Supplementary Fig. 11**. The 3D printing resolution is an important parameter in the fabrication of objects with sophisticated geometries, such as a gyroid cell, an impeller, an ammonite shell, and a skull. A square-plate-shaped object suitable for measurement of layer thickness was 3D-printed to verify the smallest possible feature size of our 3D printing system. Theoretically, a layer thickness 2–3 times the powder size provides good powder flow and spreadability[46,47]. In our system, coarse Al powder (<355 μm) was used and the minimum thickness of the 3D-printed object was about 1 mm, as indicated by the thin structures in **Figure 3b** and **Supplementary Fig. 12**. In addition to the 3D printing resolution, the bleeding issue—a phenomenon in which the binding agent solution flows out of the printed object—should also be addressed to ensure high printing quality[24]. The use of water as a solvent for the binding agent prevents this issue: it has higher vapor pressure than conventional binding agent solutions, because of which it evaporates faster and therefore prevents the solution from flowing out of the prescribed structure. Consequently, use of water ensured high dimensional accuracy of the 3D-printed objects in this study”s” and “O-Al / O” as “O-ntered.ir abbreviations used iwthin the body of the manuscript.,(for example, rewrite "f acceptable., as shown in **Figure 3c**. **Figure 3d** shows a photographic image of an as-printed 3D object and its cross-section. The high packing density of the powder by itself not only enables the 3D object to retain its shape but also promotes the solidification of the structure during the subsequent post-treatment process, thereby providing structural integrity.

Post-treatment process and several 3D-printable metals.

The post-treatment process performed for strength improvement in the standard metal BJM3DP technique can also be applied to the chelation-based metal 3D printing technique proposed herein. The post-treatment consists of a two-step process: humidification followed by thermal sintering. First, the unreacted chelator between particles was fully reacted through humidification (see **Supplementary Fig. 13** for the SEM image of the humidified 3D-printed object). Subsequent thermal sintering caused solid-state diffusion of metal particles, which led to a decrease in the interparticle porosity, as shown in **Supplementary Fig. 14**. In other words, the metal particles came into closer contact with their neighboring particles, as shown in **Figure 4a**. Consequently, the compressive strength and compressive modulus of the thermally sintered 3D-printed objects improved by factors of 4.0 and 4.7, respectively, compared to those in the as-printed state (**Figure 4b**). However, because of the issue of low intrinsic porosity in the BJM3DP technique, which arises from constrained sintering of coarse particles, the mechanical strength of the printed object is typically lower than that of objects printed by other 3D printing techniques[22]. Therefore, additional strategies to improve strength through lowering of interparticle porosity are required. It is possible to increase the packing density by using powder with an optimized particle size distribution[48]. In general, the use of bimodal powder mixtures having an appropriate coarse-to-fine

particle size ratio enables the fine particles to fill the interstitial voids between the coarse particles. Moreover, molten metal can readily infiltrate the interparticle pores of the printed object through the capillary force after the sintering process[49]. These strategies are expected to contribute to improvement in the mechanical properties of printed objects through minimization of the final porosity. **Figure 4c** shows objects 3D-printed using copper (Cu), iron (Fe), and a titanium–aluminum–vanadium alloy (Ti–6Al–4V). The successful 3D printing using various metals demonstrates that our developed 3D printing system is universally applicable to a wide variety of elemental metals and their alloys.

Discussion

An eco-friendly chelator-based binding mechanism for BJM3DP was proposed and the feasibility of the developed 3D printing system was demonstrated. Structural integrity of the 3D-printed objects was achieved through successful formation of metal-chelate bridges between the particles, and the correlation of this structural integrity with the number of coordination sites was subsequently investigated. The chemistry of chelation was used as the basis for the fabrication of various 3D objects with sophisticated geometries and high dimensional accuracy. Moreover, the mechanical properties of the 3D-printed objects were improved by reducing the interparticle porosity through a post-treatment process. Finally, 3D printing was successfully performed using various metal powders, which demonstrated the applicability of the developed printing system to various types of metals. The proposed facile approach of using environmentally friendly chelators is expected be a cornerstone for promoting the development of desktop metal 3D printing systems for domestic use.

Methods

Materials. The four chelator powders were prepared by grinding sodium ascorbate (≥99%, Sigma-Aldrich), sodium succinate (≥99%, Sigma-Aldrich), sodium tartrate (≥99%, Sigma-Aldrich), and sodium citrate (≥99%, Sigma-Aldrich). Then, each chelator powder was uniformly mixed at a concentration of 20% (w/w) with Al powder (≤40 mesh, Changsung) and then sieved through a mesh. Sodium chloride (≥99%, Sigma-Aldrich) with a concentration of 5% (w/w) was used as an additive. The preparation procedure of the other three metal powders (Cu (≤40 mesh, Sigma-Aldrich), Fe (≤325 mesh, Duksan), and Ti–6Al–4V (≤325 mesh, Grade 5, Korea Powder)) was the same as that of the metal chelator mixture.

BJM3DP process. The desktop printer for BJM3DP was assembled using a fusion deposition modeling 3D printer kit (Geeetech I3 Pro, Shenzhen Getech Co., Ltd.). An acrylic gantry box add-on set (Colorpod, Spitstec, Netherlands) was mounted on the assembled metal 3D printer. BJM3DP was performed in an environment in which room temperature (~25 °C) and 20% relative humidity were maintained. An inkjet cartridge (HP45, Hewlett-Packard) was filled with 30 mL of DI water. The printing speeds was fixed at 2000 mm min^{-1}. The temperature of both the feeder platform and the inkjet nozzle was maintained at 70 °C to control the evaporation rate of water during the 3D printing process. After the 3D printing process, the printed object was humidified by exposing it to a humidifier spraying water at a rate of 35 mL h^{-1} in a cylindrical chamber for 30 min. Subsequently, the printed object was thermally sintered in a tube furnace

(LHA-12/300, Lenton) under nitrogen and hydrogen gas flows at flow rates of 0.8 L min^{-1} and 0.2 L min^{-1}, respectively.

Characterization. The formation of a metal-chelate complex between the Al particles in the 3D-printed objects was confirmed by FT-IR spectroscopy (VERTEX 70, Bruker Corporation, Germany) and XPS analysis (ESCALAB 250Xi, Thermo-Scientific, USA). The 3D-printed objects were visualized by SEM (JEOL-7800F, JEOL, Ltd., Japan). For compression tests, objects were 3D-printed according to the ASTM E9 standard. Compression tests were performed using a universal testing machine (QC-506M2F, Cometech) with a compression rate of 8 mm s^{-1}. The interparticle porosity of the 3D-printed objects was measured by mercury intrusion porosimetry (PM33GT, Quantachrome).

Data availability

All data generated or analyzed during this study are included in this published article (and its Supplementary Information files).

Declarations

Acknowledgements

This work was supported by the Basic Science Program through the National Research Foundation (NRF) of Korea funded by the Ministry of Science and ICT, Korea (2020R1A2C2007819 and 2020R1A4A2002806) and the Korea Medical Device Development Fund grant funded by the Korea government (the Ministry of Science and ICT, the Ministry of Trade, Industry and Energy, the Ministry of Health & Welfare, the Ministry of Food and Drug Safety) (Project Number: KMDF_PR_20200901_0093, 9991006766).

Author contributions

J. H. Cho conceived the concept, designed all the experiments, and supervised the work. S. Y. Cho and D. H. Ho carried out most of the experimental work and data analysis. Y. Y. Choi assisted the data analysis with all other authors. S. Lim, S. Lee, J. W. Suk performed the mechanical property analysis of 3D printed object. All authors discussed the progress of research and contributed to editing the manuscript.

Additional Information

Supporting Information is available from https://www.nature.com/ncomms/ or from the author.

Competing interests

The other authors declare no competing interests.

References

1. Kim, S. H. et al. Precisely printable and biocompatible silk fibroin bioink for digital light processing 3D printing. *Nat. Commun.* **9**, 1620 (2018).
2. Ge, Q. et al. 3D printing of highly stretchable hydrogel with diverse UV curable polymers. *Sci. Adv.* **7**, eaba4261 (2021).
3. Giachini, P. A. G. S. et al. Additive manufacturing of cellulose-based materials with continuous, multidirectional stiffness gradients. *Sci. Adv.* **6**, eaay0929 (2020).
4. Darkes-Burkey, C. & Shepherd, R. F. High-resolution 3D printing in seconds. *Nature* **588**, 594-595 (2020).
5. Regehly, M. et al. Xolography for linear volumetric 3D printing. *Nature* **588**, 620-624 (2020).
6. Deore, B. et al. Direct printing of functional 3D objects using polymerization-induced phase separation. *Nat. Commun.* **12**, 55 (2021).
7. Kenel, C., Casati, N. P. M. & Dunand, D. C. 3D ink-extrusion additive manufacturing of CoCrFeNi high-entropy alloy micro-lattices. *Nat. Commun.* **10**, 904 (2019).
8. Zhang, D. et al. Additive manufacturing of ultrafine-grained high-strength titanium alloys. *Nature* **576**, 91-95 (2019).
9. Pollock, T. M. Alloy design for aircraft engines. *Nat. Mater.* **15**, 809-815 (2016).
10. Daly, A. C., Davidson, M. D. & Burdick, J. A. 3D bioprinting of high cell-density heterogeneous tissue models through spheroid fusion within self-healing hydrogels. *Nat. Commun.* **12**, 753 (2021).
11. Liang, K., Carmone, S., Brambilla, D. & Leroux, J.-C. 3D printing of a wearable personalized oral delivery device: A first-in-human study. *Sci. Adv.* **4**, eaat2544 (2018).
12. Robinson, S. S. et al. Patient-specific design of a soft occluder for the left atrial appendage. *Nat. Biomed. Eng.* **2**, 8-16 (2018).
13. Ho, D. H. et al. 3D-printed sugar scaffold for high-precision and highly sensitive active and passive wearable sensors. *Adv. Sci.* **7**, 1902521 (2020).
14. Gervasoni, S. et al. CANDYBOTS: A new generation of 3D-printed sugar-based transient small-scale robots. *Adv. Mater.* **32**, 2005652 (2020).
15. Jakus, A. E., Taylor, S. L., Geisendorfer, N. R., Dunand, D. C. & Shah, R. N. Metallic architectures from 3D-printed powder-based liquid inks. *Adv. Funct. Mater.* **25**, 6985-6995 (2015).
16. Taylor, S. L., Jakus, A. E., Shah, R. N. & Dunand, D. C. Iron and nickel cellular structures by sintering of 3D-printed oxide or metallic particle inks *Adv. Eng. Mater.* **19**, 1600365 (2017).

17. Reiser, A. et al. Multi-metal electrohydrodynamic redox 3D printing at the submicron scale. *Nat. Commun.* **10**, 1853 (2019).
18. Vyatskikh, A. et al. Additive manufacturing of 3D nano-architected metals. *Nat. Commun.* **9**, 593 (2018).
19. Gustmann, T. et al. Influence of processing parameters on the fabrication of a Cu-Al-Ni-Mn shape-memory alloy by selective laser melting. *Addit. Manuf.* **11**, 23-31 (2016).
20. Zhang, B. C., Dembinski, L. & Coddet, C. The study of the laser parameters and environment variables effect on mechanical properties of high compact parts elaborated by selective laser melting 316L powder. *Mater. Sci. Eng. A* **584**, 21-31 (2013).
21. Karlsson, J., Snis, A., Engqvist, H. & Lausmaa, J. Characterization and comparison of materials produced by electron beam melting (EBM) of two different Ti–6Al–4V powder fractions. *J. Mater. Process. Technol.* **213**, 2109-2118 (2013).
22. Gokuldoss, P. K., Kolla, S. & Eckert, J. Additive manufacturing processes: selective laser melting, electron beam melting and binder jetting—selection guidelines. *Materials* **10**, 672 (2017).
23. Sachs, E., Cima, M. & Cornie, J. Three-dimensional printing: Rapid tooling and prototypes directly from a CAD model. *CIRP Ann. Manuf. Technol.* **39**, 201-204 (1990).
24. Mostafaei, A. et al. Binder jet 3D printing—Process parameters, materials, properties, modeling, and challenges. *Prog. Mater. Sci.*, 100707 (2020).
25. ASTM. F2792-12a. Standard terminology for additive manufacturing technologies. (ASTM International, West Conshohocken, PA, 2012).
26. Bai, Y. & Williams, C. B. An exploration of binder jetting of copper. *Rapid Prototyp. J.* **21**, 177-185 (2015).
27. Gilmer, D. et al. An in-situ crosslinking binder for binder jet additive manufacturing. *Addit. Manuf.* **35**, 101341 (2020).
28. Levy, A., Miriyev, A., Elliott, A., Babu, S. S. & Frage, N. Additive manufacturing of complex-shaped graded TiC/steel composites. *Mater. Des.* **118**, 198-203 (2017).
29. Michaels, S., Sachs, E. M. & Cima, M. J. Metal parts generation by three dimensional printing. 1992 International Solid Freeform Fabrication Symposium. 1992).
30. Hughes, K., Meek, M. E., Walker, M., Turner, L. & Moir, D. 2-Butoxyethanol: Hazard characterization and exposure-response analysis. *J. Environ. Sci. Health, Part C: Toxicol. Carcinog.* **19**, 77-104 (2001).
31. Harreus, A. L. et al. *2-Pyrrolidone*. *Ullmann's Encyclopedia of Industrial Chemistry* (Wiley, 2011).
32. Protection of environment, 40 C.F.R. § 401.15 (2011).
33. Schafer, E. W., Bowles, W. A. & Hurlbut, J. The acute oral toxicity, repellency, and hazard potential of 998 chemicals to one or more species of wild and domestic birds. *Arch. Environ. Contam. Toxicol.* **12**, 355-382 (1983).
34. Afshar-Mohajer, N., Wu, C.-Y., Ladun, T., Rajon, D. A. & Huang, Y. Characterization of particulate matters and total VOC emissions from a binder jetting 3D printer. *Build. Environ.* **93**, 293-301 (2015).

35. Zontek, T. L., Ogle, B. R., Jankovic, J. T. & Hollenbeck, S. M. An exposure assessment of desktop 3D printing. *J. Chem. Health. Saf.* **24**, 15-25 (2017).
36. Chen, R. et al. Exposure, assessment and health hazards of particulate matter in metal additive manufacturing: A review. *Chemosphere* **259**, 127452 (2020).
37. Asemave, K. Greener chelators for recovery of metals and other applications. *Organic & Medicinal Chem IJ.* **6**, 555694 (2018).
38. Sekhara Varma, T. N. & Ramakrishnan, C. V. Biosynthesis of Citric Acid in Citrus Fruits. *Nature* **178**, 1358-1359 (1956).
39. Fraga, A. K. et al. Synthesis and characterization of aluminum citrate compounds and evaluation of their influence on the formation of hydrogels based on polyacrylamide. *Iran. Polym. J.* **29**, 649-657 (2020).
40. Papageorgiou, S. K. et al. Metal-carboxylate interactions in metal-alginate complexes studied with FTIR spectroscopy. *Carbohydr. Res.* **345**, 469-473 (2010).
41. Nakamoto, K. *Infrared and raman spectra of inorganic and coordination compounds*. *Handbook of Vibrational Spectroscopy* (Wiley, 2006).
42. Tajmirriahi, H. A. Coordination chemistry of vitamin-C . Part III. Interaction of L-ascorbic-acid with Al(III), La(III), and Pb(II) ions - Evidence for metal chelate formation in the solid and aqueous-solution. *J. Inorg. Biochem.* **44**, 39-45 (1991).
43. Sherwood, P. M. A. Introduction to studies of aluminum and its compounds by XPS. *Surf. Sci. Spectra* **5**, 1-3 (1998).
44. Wysocka, J., Krakowiak, S. & Ryl, J. Evaluation of citric acid corrosion inhibition efficiency and passivation kinetics for aluminium alloys in alkaline media by means of dynamic impedance monitoring. *Electrochim. Acta* **258**, 1463-1475 (2017).
45. Li, W., Cochell, T. & Manthiram, A. Activation of aluminum as an effective reducing agent by pitting corrosion for wet-chemical synthesis. *Sci. Rep.* **3**, 1229 (2013).
46. Butscher, A. et al. Moisture based three-dimensional printing of calcium phosphate structures for scaffold engineering. *Acta. Biomater.* **9**, 5369-5378 (2013).
47. Lu, K. & Reynolds, W. T. 3DP process for fine mesh structure printing. *Powder Technol.* **187**, 11-18 (2008).
48. Bai, Y., Wagner, G. & Williams, C. B. Effect of particle size distribution on powder packing and sintering in binder jetting additive manufacturing of metals. *J. Manuf. Sci. Eng.* **139**, 081019 (2017).
49. Cordero, Z. C., Siddel, D. H., Peter, W. H. & Elliott, A. M. Strengthening of ferrous binder jet 3D printed components through bronze infiltration. *Addit. Manuf.* **15**, 87-92 (2017).

Figures

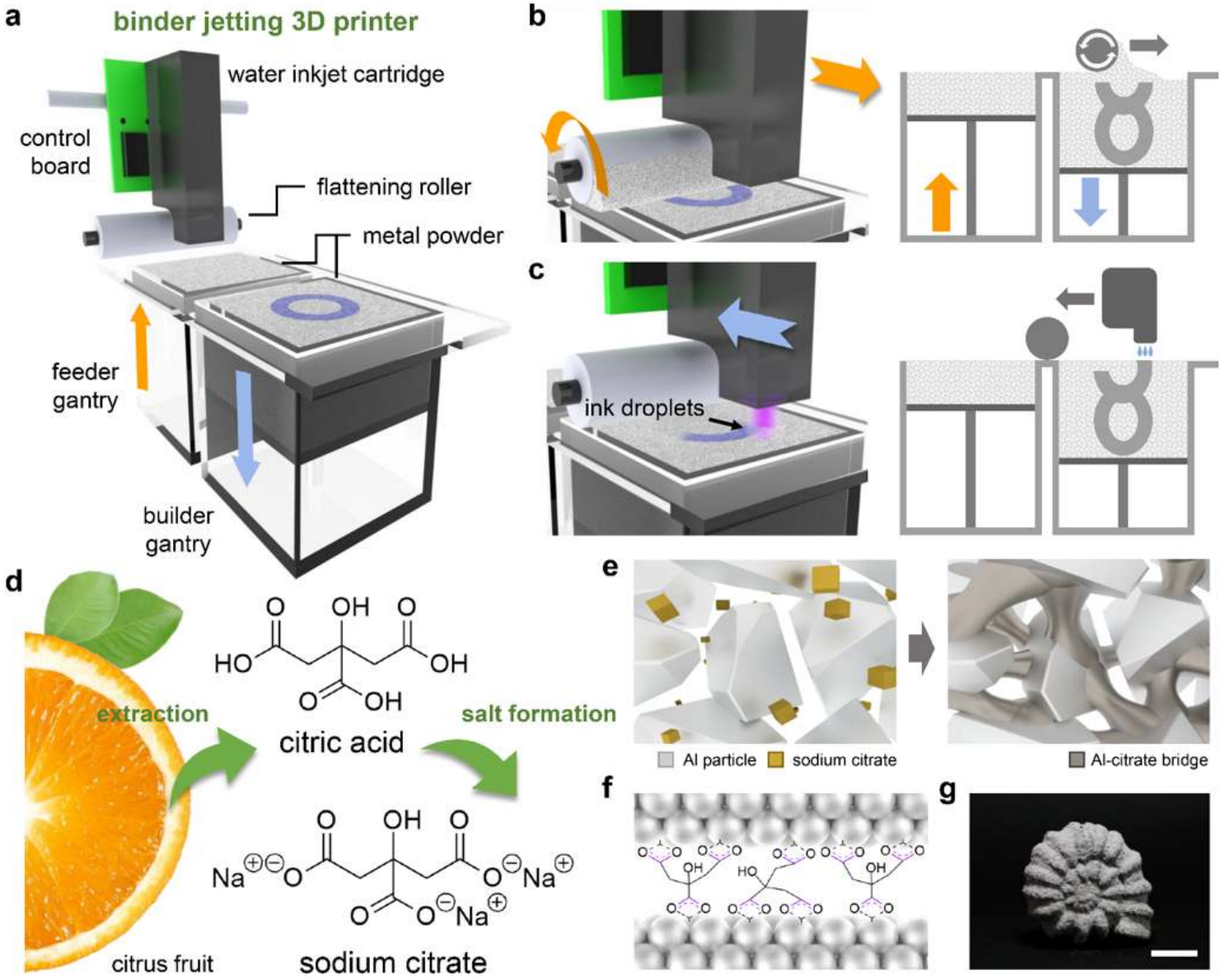

Figure 1

Eco-friendly BJM3DP. a Schematic illustration of BJM3DP system. b Powder layer deposition on builder gantry box. c Programmed water ink-jetting onto powder layer. d Chemical structures of naturally available eco-friendly fruit acid (top) and its sodium salt (bottom). e Schematic description of as-prepared mixture of metal powder and chelator (left) and metal-chelate bridge formation after metal chelation (right). f Chemical structure of metal-chelate bridges on metal particle surface. g Photographic image of 3D-printed ammonite-shell-shaped object (scale bar: 10 mm).

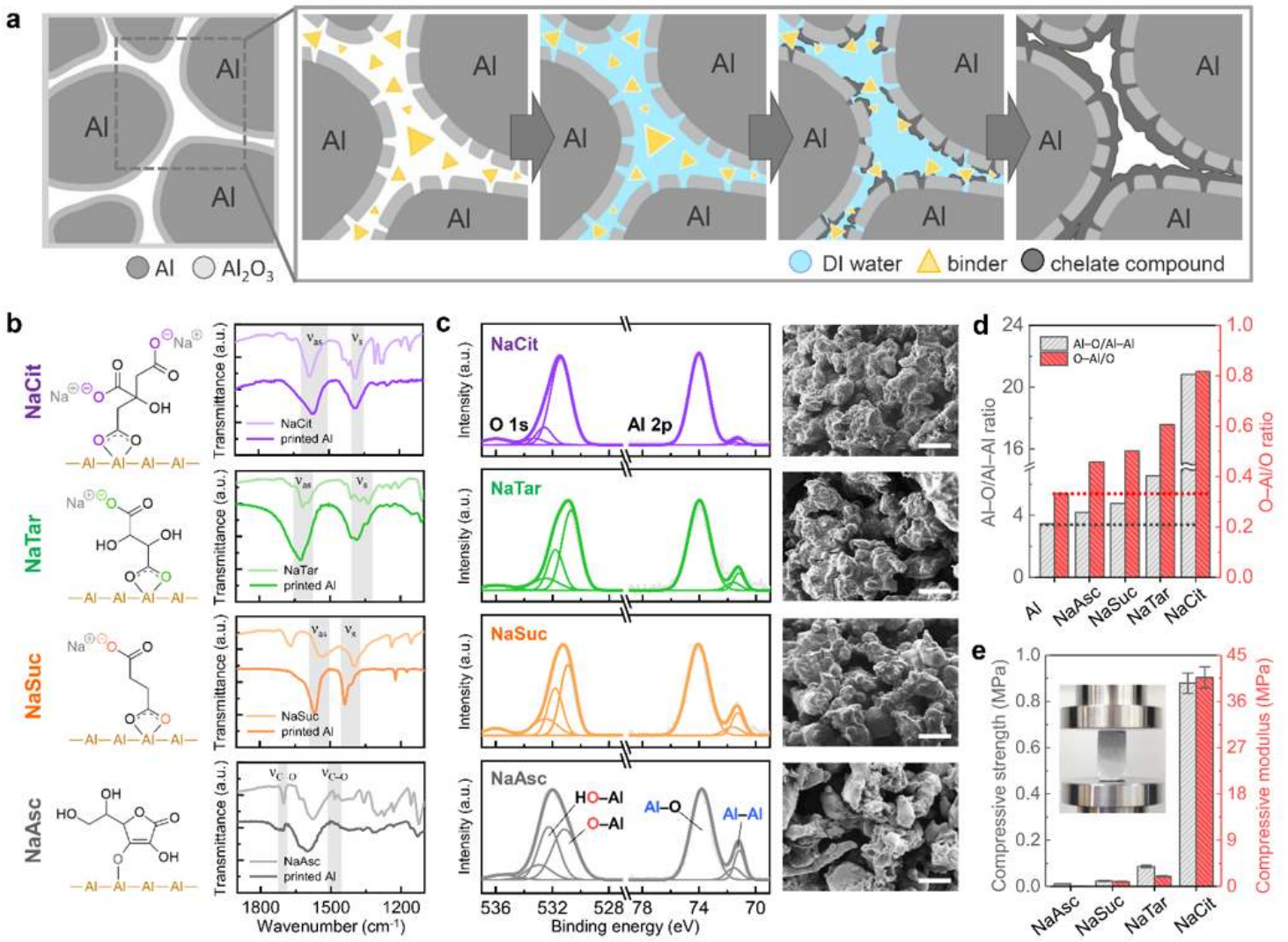

Figure 2

Formation of metal-chelate bridges between metal particles. a Schematic illustration of mechanism of metal chelation on metal particle surface. b Chemical structures of chelators and their coordination with metal particle surface (left) and FT-IR analysis with identified vibration peaks (right). c Deconvoluted XPS peaks (left) and cross-sectional SEM images of chelated metal particle surface (right) (scale bar: 100 μm). d Al–O/Al–Al atomic ratio (integrated areas of peaks in Al 2p spectra) and O–Al/O atomic ratio (integrated areas of peaks in O 1s spectra) for various chelators. e Compressive strength and modulus of objects 3D-printed by BJM3DP using various chelators. The inset shows a photographic image of compression testing of the 3D-printed object.

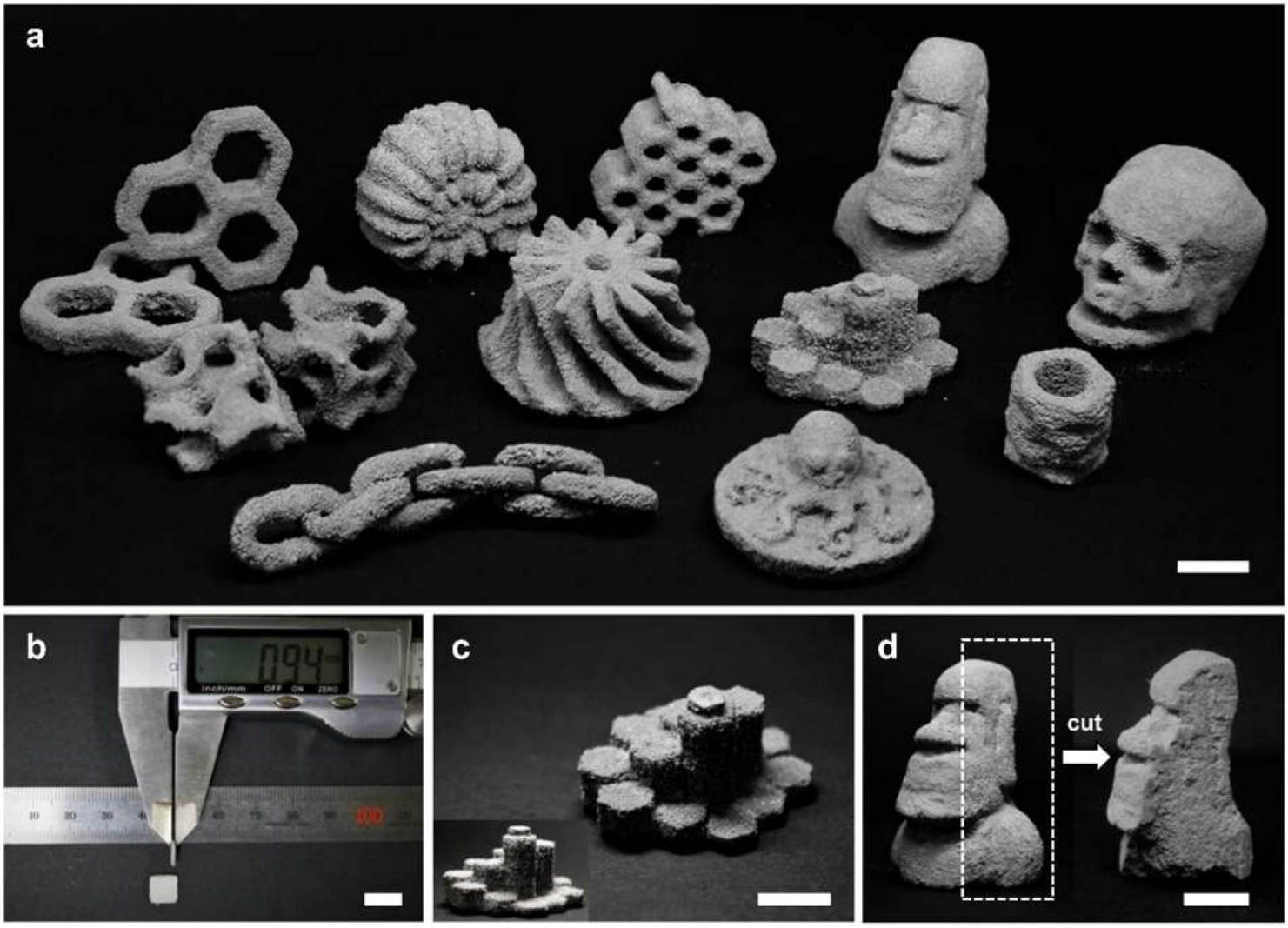

Figure 3

Various objects 3D-printed using NaCit chelator. Photographic images of a 3D-printed Al objects having various shapes (scale bar: 10 mm). b–d Photographic images of representative 3D-printed objects, which depict their b 3D-printable feature size, c high dimensional accuracy, and d high packing density (scale bar: 10 mm). Three-dimensional model data for the ammonite shell (thing: 1611970), moai statue (thing: 3905999), octopus (thing: 159217), gyroid cube (thing: 757884), skull (thing: 11953), hexagon stair sculpture (thing: 46966), and faceted cup (thing: 414252) were acquired from the open-source website www.thingverse.com. Other 3D models were designed by the authors using Fusion 360 software.

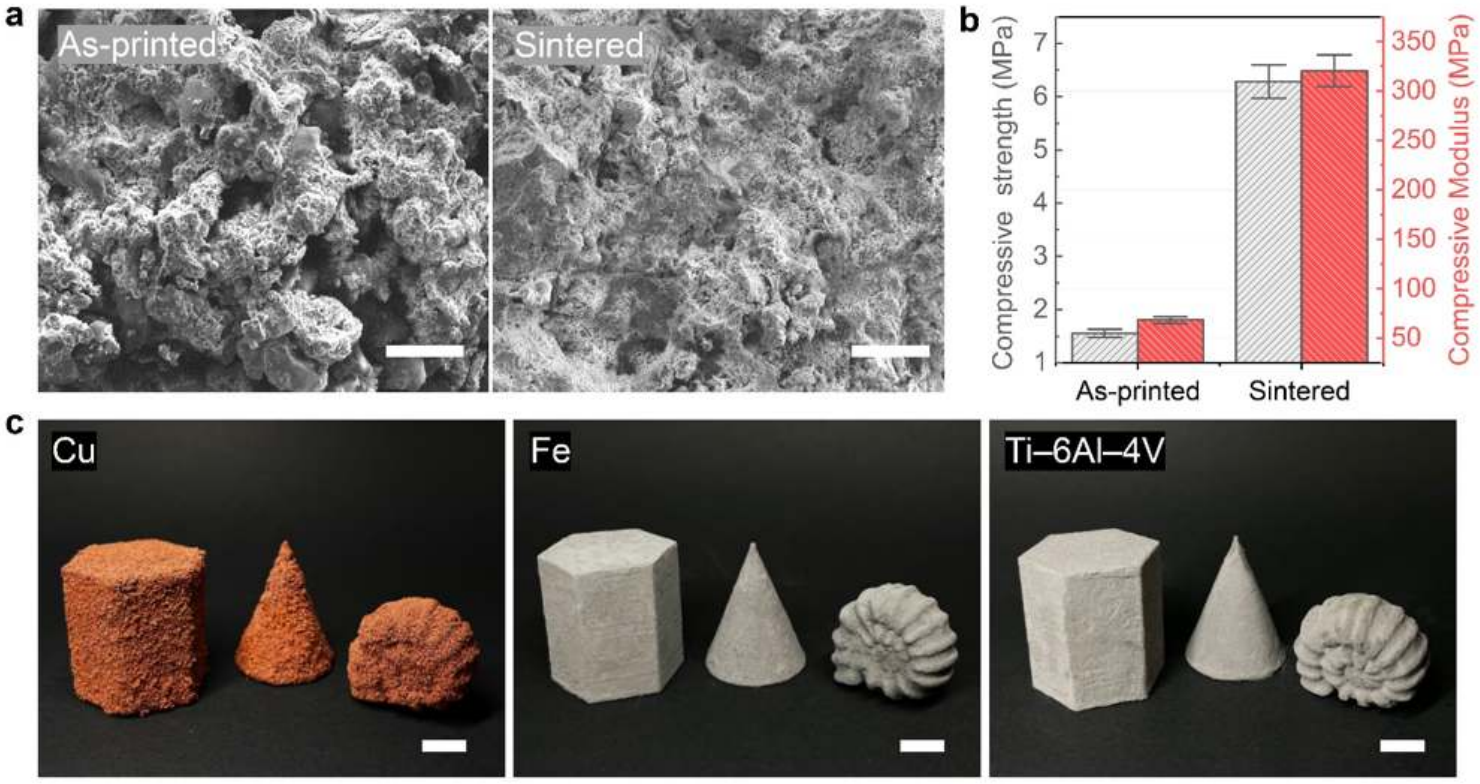

Figure 4

Post-treatment process and several 3D-printable metals. a Cross-sectional SEM images of as-printed 3D object (left) and sintered 3D object (right) (scale bar: 100 μm). b Comparison of compressive strength and modulus of as-printed 3D object and sintered 3D object. c Photographic images of objects 3D-printed using Cu (left), Fe (middle), and Ti–6Al–4V alloy (right) (scale bar: 10 mm).

Supplementary Files

This is a list of supplementary files associated with this preprint. Click to download.

- SupportingInformationJHCHO.doc